Hybrid Optical-Acoustic Calibration and Validation of Ionacoustic Dosimetry in Laser-Driven Proton Beams

M. Maxouti*[1,2,3], P.R. Hobson[4], O. Jeremy[1], C. Dyson[1], B. Cox[5], N. Dover[1], S. Gerlach[6], J. Lascaud[6], Z. Sadur[1], N. Zakhir[1], C. Burn[7], X. Chen[1], R.A. Amos[5], C. Whyte[8], J. Schreiber[6], K. Parodi[6], J.C. Bamber[9], K. Long[1,2,3]

[1] Department of Physics, Imperial College London, UK;
[2] John Adams Institute for Accelerator Science, UK;
[3] Particle Physics Department, STFC Rutherford Appleton Laboratory, UK;
[4] School of Physical and Chemical Sciences, Queen Mary University of London, UK;
[5] Department of Medical Physics and Biomedical Engineering, University College London, UK;
[6] Department of Medical Physics, Ludwig-Maximilians-Universität München, Germany;
[7] School of Physics Astronomy - University of Birmingham, UK;
[8] Department of Physics, University of Strathclyde, UK;
[9] Institute of Cancer Research and Royal Marsden NHS Foundation Trust, UK

Abstract

The SmartPhantom is a novel detector developed for real-time three-dimensional dosimetry in particle therapy using pulsed proton and light-ion beams. The system integrates the detection of ion-induced acoustic signals with optical readout using a liquid scintillator. A detailed simulation pipeline using BDSIM, Geant4, k-Wave and Ansys Zemax OpticStudio have been performed alongside experimental validation at the MC40 cyclotron at the University of Birmingham and the Laser-driven Ion Acceleration (LION) beamline at the Centre for Advanced Laser Applications (CALA). The SmartPhantom's performance is evaluated in terms of energy resolution, beam characterization, response linearity, and spatial reconstruction accuracy, demonstrating its potential as a powerful tool for advanced ion beam dosimetry.

1 Introduction

Cancer is the second leading cause of death globally, with radiotherapy treating about 50% of cancer patients [1]. Conventional radiotherapy uses photons (x-rays), however it often irradiates healthy cells surrounding the cancerous region. New cancer treatment facilities use protons and light ions for their ability to deposit maximum dose in a small tissue volume at the end of their range [2].

To enable next-generation therapy, the *Laser-hybrid Accelerator for Radiobiological Applications (LhARA)* has been proposed [3]. LhARA aims to advance radiobiological research by exploring the therapeutic benefits and biological responses of different particle beam characteristics [3]. Using pulsed proton and light-ion beams, LhARA will deliver a variety of different ions, beam widths, pulse durations and repetition rates, flexibly and precisely. To minimize uncertainties in dose delivery, accurate real-time monitoring is essential; however, current techniques such as PET and prompt gamma imaging lack the spatial and temporal resolution required for this purpose [4, 5].

This work presents the *SmartPhantom*, a novel detector designed to monitor the three-dimensional dose accumulation from pulsed ion beams on the nanosecond timescale, such as those to be produced by LhARA and other laser-driven accelerators. The proposed instrumentation introduces novel capabilities, such as providing calibrated feedback, unlike other monitoring devices that provide a relative, not an absolute, determination of the dose delivered. The SmartPhantom achieves that by enabling simultaneous ionoacoustic and optical measurement of the energy deposition distribution within a liquid scintillator.

1.1 Particle Therapy and the Bragg Peak

Conventional radiotherapy uses x-rays (photons) to target and destroy the tumour region. While photons effectively damage cancerous cells, their energy is not confined to the tumor; instead, they

*m.maxouti21@imperial.ac.uk

deposit dose along their entire path through the body. This exposes healthy tissue before and beyond the tumor, potentially causing unwanted side effects [2].

In contrast, proton and light-ion radiotherapy has emerged as an advanced alternative in cancer treatment due to the particles' unique physical properties. When ions interact with matter, they gradually lose energy, slowing down and depositing an increasing amount of energy over a shorter distance. This culminates in a pronounced peak in energy deposition near the end of their range, known as the *Bragg Peak*, and hence the effect on the healthy tissue surrounding the tumour is minimized [6].

The Bragg Peak enables precise delivery of maximum dose within the tumor while sparing surrounding healthy tissue from excess radiation. This characteristic not only improves tumor control, but also reduces side effects and damage to nearby critical structures [6]. As a result, proton and ion beam therapies are increasingly adopted in modern cancer treatment, including LhARA, marking a major advance in radiotherapy precision and safety.

1.2 The Laser-Hybrid Accelerator for Radiobiological Applications (LhARA)

LhARA, the Laser-hybrid Accelerator for Radiobiological Applications, is designed to advance technologies that can enhance the clinical use of radiotherapy [3]. It will use proton and light ion beams to study radiobiological effects and the impact of ionising radiation on tissue, enabling particle-beam therapy to be delivered in new regimens. The LhARA facility will be significantly smaller, more cost-effective, and more flexible than current facilities, with an extended range of beam characteristics. Its triggerable source and highly automated accelerator design would make patient-specific treatment feasible.

The beam will be generated using a thin foil target and a powerful pulsed laser. The laser-driven particles will be captured and focused into a large flux using Gabor (electron plasma) lenses [7]. This setup allows for a wide variety of time structures, spectral distributions, and spatial configurations, enabling the delivery of instantaneous dose rates ($\geq$ 40 Gy/s) and ions in the mini- and micro- beam range [8]. The LhARA accelerator will have three end stations. The first, low-energy end station (Stage 1) will deliver proton beams at 10–15 MeV for *in vitro* radiobiological studies. Post-acceleration will be achieved using fixed-field alternating-gradient acceleration (FFA), with the beam reaching the *in vitro* and *in vivo* high-energy end stations (Stage 2) at proton energies up to 127 MeV or ions up to 33 MeV per nucleon.

1.3 The Ionacoustic Process

As the ion beam transverses a medium, it interacts via Coulomb scatterings, transferring its kinetic energy to the atoms in the form of heat. If the ion pulse duration is significantly shorter than the medium's stress relaxation time, the energy remains confined within the system. This condition, commonly referred to as the stress-confinement criterion, leads to a rapid increase in temperature [9]. Assuming that the temperature rise is short enough to neglect thermal diffusion, the energy is converted into mechanical stress in the form of an acoustic (ultrasound) wave.

The source pressure distribution at position $\mathbf{r}$ and temperature T, denoted as $p_0(\mathbf{r}, T)$, can be derived from the energy deposition distribution $E(\mathbf{r}, T)$ according to

$$p_0(\mathbf{r}, T) = \Gamma(\mathbf{r}, T) \times E(\mathbf{r}, T), \tag{1}$$

where $\Gamma(\mathbf{r}, T)$ is the dimensionless Grüneisen coefficient, representing the efficiency of converting absorbed heat energy into pressure [10]. The Grüneisen coefficient is defined as

$$\Gamma(\mathbf{r}, T) = \frac{v_s^2 \beta}{C_p}, \tag{2}$$

with v_s being the speed of sound in the medium, β the thermal expansion coefficient, and C_p the specific heat capacity at constant pressure.

These waves can be detected by ultrasound transducers, providing time-series data that enable the reconstruction of the spatial and temporal distribution of the source causing them. Due to the high speed of ultrasound in various media, signals are detected almost instantaneously [11].

1.4 Real-Time Dosimetry with the SmartPhantom

LhARA's ultra-short pulses (10–40 ns) satisfy the stress-confinement condition, making them ideal for generating ion-acoustic waves. Although standard ultrasound transducers detect only relative dose, the

SmartPhantom enables absolute determination by using a liquid scintillator as the propagation medium [12]. The key innovation lies in using the schitllator's optical response, which is proportional to the local energy deposition, as an internal reference for calibrating the acoustic signal. This enables quantitative interpretation of the acoustic signal and real-time, pulse-by-pulse 3D dose mapping.

To validate this concept, we investigate two core hypotheses. First, we assess whether ionoacoustic signals can be absolutely calibrated in real time using the optical output as a reference. Second, we examine the spatial and quantitative correlation between acoustic and optical dose profiles under pulsed, laser-driven proton beams. These capabilities were experimentally validated at the *Laser-driven Ion Acceleration (LION)* beamline at the Centre for Advanced Laser Applications (CALA), where the SmartPhantom demonstrated the first fully integrated system capable of simultaneous, real-time ionoacoustic and optical characterization of pulsed ion beams [13].

1.5 The Laser-driven Ion Acceleration (LION)

The Laser-driven Ion Acceleration (LION) facility produces a high flux of protons by directing a powerful laser onto a thin foil target. This proton source is driven by the ATLAS 3000 laser, a high-intensity, 2.5 PW Titanium:Sapphire (Ti:Sa) system [14]. The laser delivers ultra-short pulses of up to 25 fs duration and 60 J of energy, making it highly effective for generating ion-acoustic waves.

1.5.1 Proton Source

Due to the extremely high intensity of the laser ($> 10^{18}$ W/cm^2), the front surface of the foil is rapidly ionized, creating a pre-plasma with a steep density gradient. The intense interaction between the laser pulse and the plasma accelerates electrons via the Lorentz force, driving them toward the foil's rear (non-irradiated) surface. Because of the large mass difference between electrons and ions, the electrons move much faster and can escape the foil, establishing a strong electrostatic sheath.

These highly energetic electrons escaping the foil generate a potential difference perpendicular to the target surface, which traps the remaining electrons. This leaves a net positive charge on the rear surface, resulting in a charge separation field. This field further ionizes atoms, which originate mainly from water vapor, hydrocarbons, and oxide contaminants on the target surface [15]. The ions are then accelerated to high speeds, exiting the foil normal to its surface, driven by the direction of the charge-separation field. This process is known as Target Normal Sheath Acceleration (TNSA).

1.5.2 Collimation and Downstream Propagation

The LION beamline features a quadrupole doublet composed of two orthogonally arranged permanent magnet quadrupoles. The first quadrupole has a length of 40 mm and a measured magnetic field gradient of 332±13 T/m, while the second measures 20 mm and has a measured magnetic field gradient of 334±13 T/m. Both have a 10 mm bore and a total outer diameter of 50 mm [16]. The drift lengths between the quadrupoles are optimized and adjusted using a motorized stage to magnetically focus specific beam energies downstream. The total length from the target to the exit window is 1.845 m and operates in vacuum. A schematic diagram of the LION beamline is shown in Figure 1.

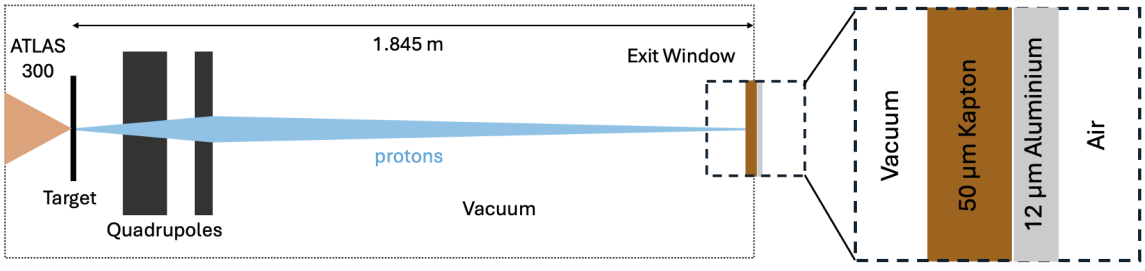

Figure 1: Schematic diagram of the LION beamline featuring the permanent quadrupole doublet focusing mechanism and beamline element configuration.

After the exit window, the particles travel through air towards the detector. The LION beamline exit window consists of a 50 μm Kapton® (polyimide) foil and a 12 μm aluminium foil; a combination

that effectively stops protons up to 2.1 MeV. In addition, the quadrupoles' limited aperture blocks some source-generated particles, and those reaching the magnet bore can cause severe damage. To prevent this, an elliptical aluminum shielding plate is placed in the front.

Table 1 summarizes the drift lengths required to focus protons with modal energies between 10 and 20 MeV. Here, Drift 1 is the distance from the source to the first quadrupole, Drift 2 is between the two quadrupoles, and Drift 3 spans from the second quadrupole to the exit window.

Table 1: Ideal drift lengths to focus different beam energies at the LION beamline.

Energy [MeV]	**Drift 1 [mm]**	**Q1 Tilt [°]**	**Drift 2 [mm]**	**Q2 Tilt [°]**	**Drift 3 [mm]**
10	42.28	0	27.20	0	1715.52
12	46.94	0	32.31	0	1705.75
14	51.24	0	37.09	0	1696.67
16	55.24	0	41.62	0	1688.14
18	59.00	0	45.94	0	1680.06
20	62.56	0	50.08	0	1672.36

2 The SmartPhantom

2.1 Mechanical Layout

The layout of the SmartPhantom is illustrated in Figure 2. The SmartPhantom has a cuboid structure with 5 mm thick aluminium walls, and an inner volume measuring 100 mm per side. The interior is filled with a commercially available liquid scintillator, discussed in Section 2.3.1, that serves as a beam energy absorber and propagating medium. The beam enters through a 15 mm diameter air-filled cylindrical window sealed with a 50 μm black Kapton foil.

The design features four windows: two for mounting optical systems and two for acoustic transducers. The optical windows, made of 5 mm thick BK7 glass, are mounted perpendicularly to capture scintillation light from the top and side. The transducer windows are also orthogonal: one opposite the beam entrance and the other opposite the side optical window. Both are sealed with black Kapton foils to reduce internal light reflections, and for the same reason, the entire detector was anodised black.

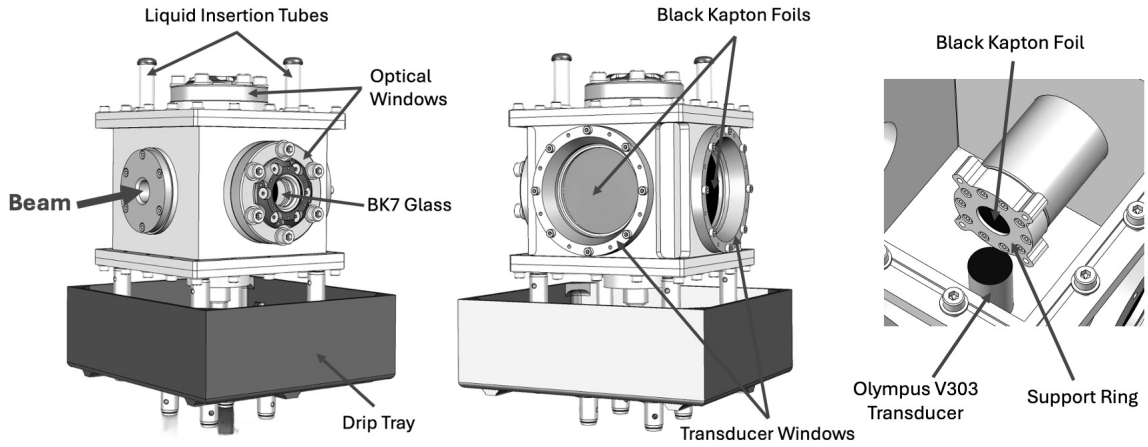

Figure 2: Layout of the SmartPhantom, featuring four windows for mounting optical and acoustic systems. Left: front view. Middle: rear view. Right: Interior view.

2.2 Acoustic Detection System

The ion-acoustic signals generated by the pulsed ion beam as it propagates through the SmartPhantom are detected using ultrasound transducers. For the evaluation conducted at the LION beamline,

the Olympus V303 transducer and the PreciFor the LION beamline evaluation, the **Olympus V303 transducer** and **Precision Acoustics ML4X50 hydrophone** were selected.

The Olympus V303 is a narrow-band piezoelectric ceramic transducer with a single 13 mm flat circular element [17]. It has a center frequency of 1 MHz, 60% bandwidth, and a stainless steel housing. The transducer face is positioned 24.9 mm from the SmartPhantom's center, perpendicular to the beam axis. The ML4X50 piston hydrophone is a high-sensitivity, broadband, single-element transducer with a 23 mm aperture [18]. It provides a flat frequency response from 300 kHz to 10 MHz, enabling detection downstream of the Bragg peak, including the plateau region.

To amplify the weak piezoelectric signals, two FEMTO® amplifiers were used: a voltage amplifier (HVA-10M-60-B) connected to the piston hydrophone, and a charge amplifier (HQA-15M-10T) paired with the Olympus V303 transducer [19, 20]. The key features of the acoustic detection systems are summarized in Table 2.

Table 2: Comparison of transducer properties used in the SmartPhantom experiments.

Feature	Olympus V303 Transducer	PA ML4X50 Hydrophone
Element Diameter	13 mm	23 mm
Frequency Range	1 MHz (60% BW)	300 kHz – 10 MHz
Positioning	24.9 mm from center, perpendicular	Flexible, downstream of Bragg peak
Amplifier Model	FEMTO HQA-15M-10T	FEMTO HVA-10M-60-B
Amplifier Specifications	15 pC/V, 10 MHz BW	10 V/mV, 60 MHz BW

2.3 Optical Imaging

Imaging of scintillation light produced by the proton beam in the liquid scintillator is provided by two identical optical systems which are orthogonal to each other and aligned with the centre of the volume. Each optical system relays the light to the CMOS sensor in a FLIR CM3-U3-31S4M-CS monochrome camera (2048 × 1536 3.45 μm square pixels).

2.3.1 Ultima Gold XR

We use the liquid scintillator Ultima Gold XR (Revvity Inc [21]) which has diisopropylnaphthalenes as its major component plus a number of fluorescent compounds that produce and wavelength-shift the scintillation light to a peak at 427 nm [22]. Its density is 0.96 gcm^{-3} and has a refractive index of 1.555 at 435.8 nm [23]. Ultima Gold XR has a light yield of approximately 11200 photons per deposited MeV.

Acoustic Properties An experiment showed that the acoustic attenuation coefficient of Ultima Gold XR at 21.8°C follows the relation

$$\alpha(f) = (0.19 \pm 0.002)\, f^{\,1.75\pm0.01} \quad \text{dB/cm},$$

where f is the frequency in the range 1.5–3.5 MHz, and the uncertainties correspond to ±1 standard deviation [**IEEE˙paper**]. In addition, the speed of sound was measured as

$$c = 1479.1 \pm 1.1\,\text{m/s},$$

with the error estimated from half the range of observed values. These values were therefore employed in the simulation discussed in Section 4.

2.3.2 Imaging Optics

Figure 3 shows the system used to effectively capture and image the emitted scintillation light. A 5 mm thick N-BK7 glass flat separates the interior volume of the SmartPhantom from the outside air, as indicated in Figure 2. Following this is a lens assembled from two identical achromatic lenses (Edmund Optics #47-638) each with a focal length of 60 mm and an outside diameter of 25 mm. These were inserted as a back-to-back pair to provide an approximate 1:1 conjugate system with symmetry about the central stop of 6 mm diameter. Using a symmetric configuration corrects for coma, distortion and lateral colour. In addition, using achromatic doublets provides correction for axial chromatic and spherical aberrations. To ensure that the images are not saturated, a thin Neutral Density (ND) filter is positioned right after the doublet, before focusing onto the CMOS sensor.

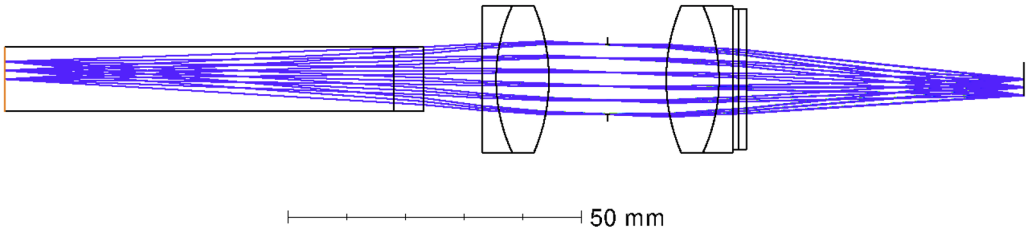

Figure 3: The imaging optical system layout. The first volume is the liquid scintillator, then the N-BK7 window. A thin ND filter is shown located just to the right of the second achromatic doublet. The fields shown are at 0, 1.5 and 3 degrees.

Lastly, the encircled energy for the three field positions (0, 1.5 and 3 degrees) is shown in Figure 4. The system performs best on the on-axis (0.0 mm), with energy tightly concentrated in a smaller radius, while performance decreases toward the edge of the field, where energy is more spread out due to off-axis aberrations. This indicates increasing image blur at larger field angles, however, even at 3.0 mm radius, the encircled energy reaches nearly 100% at around 100 μm radius.

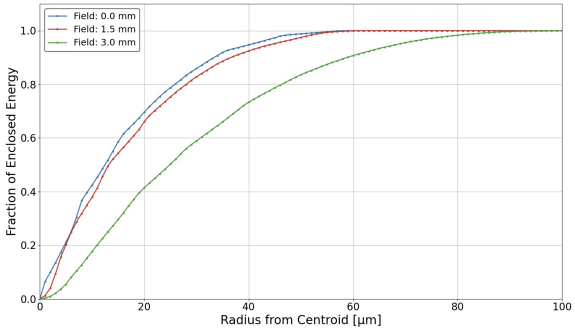

Figure 4: Encircled energy for three field positions as a function of radius from the centroid.

3 Experimental Setup and Methodology

3.1 Optical Response and Saturation

The linearity and saturation behavior of the liquid scintillator were investigated using proton beams with energies ranging from approximately 18 to 27 MeV, delivered by the MC40 cyclotron at the University of Birmingham [24]. This study aimed to characterize the response of Ultima Gold XR as a function of particle count, and thus deposited energy, in order to identify the threshold at which image saturation occurs using the imaging system described in Section 2.3.2. In addition, the experiment sought to evaluate whether the scintillator response remains linear within the expected operating range.

In the experiment, the imaging system was mounted on the side glass window of the SmartPhantom. The proton count in the beam was varied, up to approximately 96 million per camera exposure, by adjusting the cyclotron current.

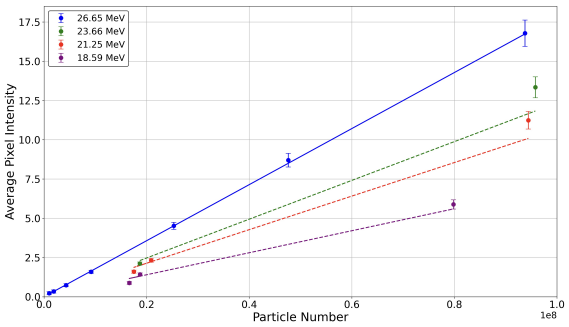

Figure 5: Average image pixel intensity against particle proton number at various proton energies.

To investigate the energy dependence of the scintillator response, Perspex (PMMA) sheets of thickness 1, 2, and 3 mm were placed at the cyclotron exit, reducing the beam energy from 26.65 MeV to 23.66, 21.25, and 18.59 MeV, respectively. In addition, a 2 mm collimator was used.

The images were corrected for background noise, averaged per configuration, and their mean pixel intensity was calculated. The results are shown in Figure 5. To ensure consistency, the camera exposure time was kept constant at 0.2 seconds throughout all measurements.

The results demonstrate that the liquid scintillator exhibits a linear response across the range of proton energies and particle counts investigated. This linearity confirms the scintillator's suitability for quantitative beam imaging, provided that the particle count remains below the saturation threshold, which, for the energies studied, appears to exceed 98 million protons.

3.2 LION Beamline Deployment

The SmartPhantom was filled with Ultima Gold XR and two imaging systems were securely mounted onto the optical flanges. To prevent image saturation, $\times 10$ neutral density filters were placed after the achromatic doublets within the imaging systems, as shown in Figure 3.

The piston hydrophone was affixed to the Kapton window opposite the entrance window, while the Olympus V303 transducer was mounted inside the SmartPhantom, immersed in the liquid scintillator at the bottom. To minimize movement and ensure proper alignment, both transducers were 3D-scanned, and custom casings were printed to provide a precise fit. In addition, a thin layer of acoustic gel was applied between the piston hydrophone and the black Kapton foil to ensure efficient acoustic coupling and signal transmission.

The SmartPhantom was mounted on a motorized translation stage and aligned with the beam axis. Images of the experimental setup are shown in Figure 6. To investigate the influence of beam width on both scintillation light and acoustic waveforms, collimators with diameters of 2 mm and 4 mm were placed between the accelerator's exit window and the SmartPhantom's entrance window. The configuration with the 2 mm collimator was tested on Day 1 of the experiment, while the 4 mm configuration was tested on Day 2, during which the quadrupoles were realigned, resulting in slightly different settings.

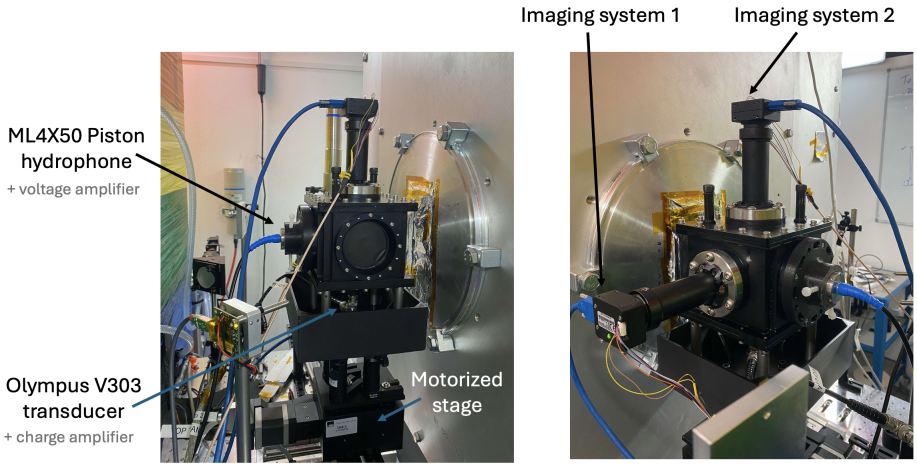

Figure 6: Experimental setup showing the SmartPhantom positioned at the LION beamline's exit window. The Piston hydrophone is aligned with the beam axis and the Olympus V303 transducer is fixed at the bottom. The two imaging systems are positioned orthogonally on the remaining sides.

3.2.1 Electronics and Data Acquisition

To enable synchronous data collection within the very short duration of the pulse, a Data Acquisition (DAQ) system was designed. The system uses an existing trigger box that receives the photodiode-detected laser signal and distributes it with negligible delay. Each camera receives a trigger pulse via a General Purpose Input/Output (GPIO) connector. The camera shutters open and close during the trigger window, ensuring that the images capture the scintillation light within the timeframe in which the beam transverses the SmartPhantom.

The Olympus V303 transducer and Piston hydrophone connect to a multichannel Picoscope 6404D, with the amplifiers in between [25]. A single trigger signal is sent from the trigger box to the picoscope, which activates the two transducers simultaneously. Similarly to the optical readout, the acoustic data are recorded only during the trigger window. The captured images and recorded acoustic signals are transmitted to the central computer along with timestamps to enable pulse-to-pulse comparison.

3.2.2 Radiochromic Films

The shape and depth-dose profiles of particles in the proton bunch were measured using 28 μm-thick RadioChromic Films (RCFs) positioned a few cm from the exit window [26]. Two RCF stacks were prepared, composed of 18 film layers each, and were irradiated on two different days with slightly different quadrupole settings. Stack A was exposed to beam radiation with design energies of 20 MeV, 20 MeV (repeat), 16 MeV and 12 MeV on Day 1. Stack B was irradiated with design energies of 18 MeV, 14 MeV, 10 MeV and 10 MeV (repeat) on Day 2. The radiochromic films were scanned with an EPSON Expression 1100 XL Pro scanner a few hours post-irradiation. To determine depth-dose profiles, the films were corrected for potential displacement within the RCF holder using geometric features.

3.2.3 Depth-Dose Curves

The RCF scans were converted to dose maps using a calibration performed with a clinical photon beam [27]. To account for scattered background radiation from the laser-driven ion source, background subtraction was performed on a layer-by-layer basis. To do this, the dose in peripheral regions of the image, well outside the area irradiated by the proton beam, was averaged and then subtracted from the entire image. Finally, the dose values were summed across all layers to generate a spatially integrated depth-dose curve, in which the depths represent the active layers of the radiochromic film stack.

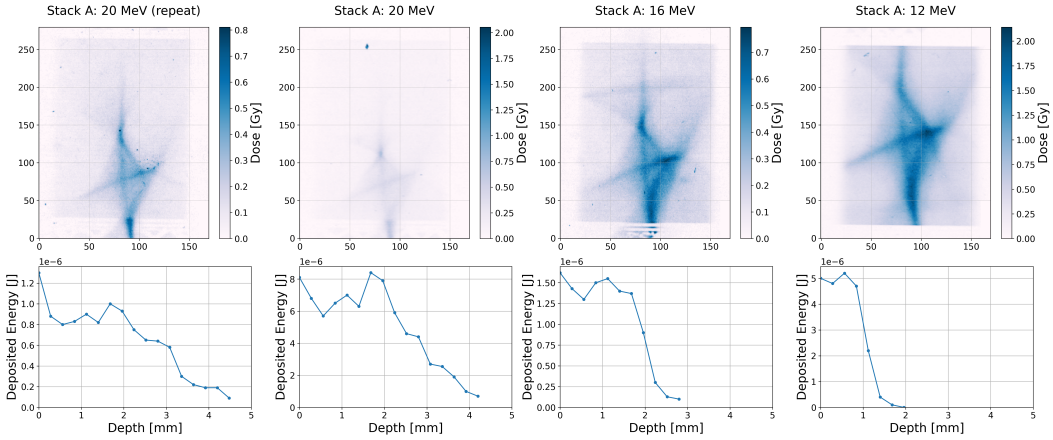

Figure 7: Depth-dose curves calculated by integrating the deposited energy within the irradiated sections across each layer of RCF Stack A.

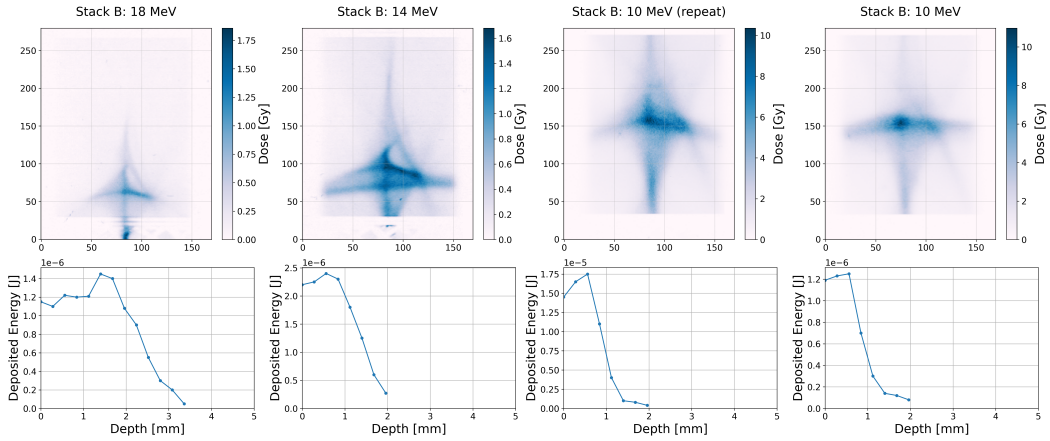

Figure 8: Depth-dose curves calculated by integrating the deposited energy within the irradiated sections across each layer of RCF Stack B.

The results for Holder A and Holder B are displayed in Figures 7 and 8, respectively. The plots reveal that beams with higher design energies penetrate deeper into the stack, as expected due to their lower stopping power, which enables them to travel further before coming to rest.

In addition, the plots show that the deposited energy decreases as the proton beams penetrate deeper into the RCF layers. However, the curves do not resemble the characteristic Bragg peak shape, where the deposited energy is lower at the entry point, steadily increasing to a peak and then sharply falls off. The observed patterns suggest that each beam is composed of particles with a wide range of energies, where each one gives its own distinct peak, resulting in a more complex overall shape. This can be attributed to slight misalignments or deviations from the ideal quadrupole settings during beamline deployment.

4 Simulation Framework

A simulation framework was established to undestand the shapes of the focused beams and the resulting scintillation patterns and acoustic signals. The simulation followed a detailed pipeline, from the particle source through to optical and acoustic detection.

4.1 LION Beamline

4.1.1 TNSA Modeling and Energy Spectrum

Several analytical equations were used to simulate the particle distribution at the source, incorporating the laser and foil target specifications at the LION beamline. The energy spectrum and angular distribution of the proton bunch have been parameterized separately.

The typical kinetic energy spectrum produced in target-normal sheath acceleration falls exponentially with kinetic energy before dropping rapidly to zero at a maximum "cut-off" energy K_{max}. The kinetic-energy spectrum of the TNSA model presented in [15] is given by

$$\frac{dN}{dK} = \frac{\mathcal{N}}{\sqrt{2KT_e}} \exp\left(-\sqrt{\frac{2K}{T_e}}\right) , \tag{3}$$

where N is the number of protons or ions produced per unit solid angle, K is the ion kinetic energy, T_e is the hot electron temperature, and $\mathcal{N}$ is a normalisation constant that depends on the laser-pulse duration.

Equation 3 is based on time-limited fluid-dynamical models which are unable to predict the cut-off kinetic energy accurately. The cut-off energy is taken to be that given by the model described in [28] in which the time over which the laser pulse creates the conditions necessary for acceleration is derived. The kinetic energy cut-off is given by

$$K_{max} = X^2 K_{i,\infty} , \tag{4}$$

where X is obtained by solving

$$\frac{t_{\text{laser}}}{t_0} = X\left(1 + \frac{1}{2}\frac{1}{1-X^2}\right) + \frac{1}{4}\ln\left(\frac{1+X}{1-X}\right) . \tag{5}$$

Here t_0 is the time over which the ion acceleration may be treated as ballistic and $K_{i,\infty}$ is the maximum possible kinetic energy that could be imparted by the electric field strength of the laser.

A Monte Carlo algorithm using the accept-reject method was implemented in Python to generate and sample protons from the energy spectrum in Eq. 3 [29, 30]. Figure **??** shows the theoretical and sampled spectra.

The energy distribution of the particles follows an exponential shape, which can be explained by the electric field established during the process. Because of the thermal distribution of the accelerated electrons, the resulting electric field also follows the same distribution. Consequently, the electron sheath decays exponentially with distance from the target, leading to the accelerated ions gaining energies following the exponential spectrum. In addition, the broadness of the distribution can be understood by the variations of the electric field in the radial and longitudinal directions. Ions found at different depths experience different ionization and acceleration strengths.

4.1.2 Angular and Spatial Distribution

The angular distribution of the flux of protons and ions produced by the TNSA mechanism has been observed as a cone centred on the normal to the foil surface [**radiochromic˙film**]. This cone has an opening angle, 2α, which varies as a function of energy, where the envelope angle α is defined such that

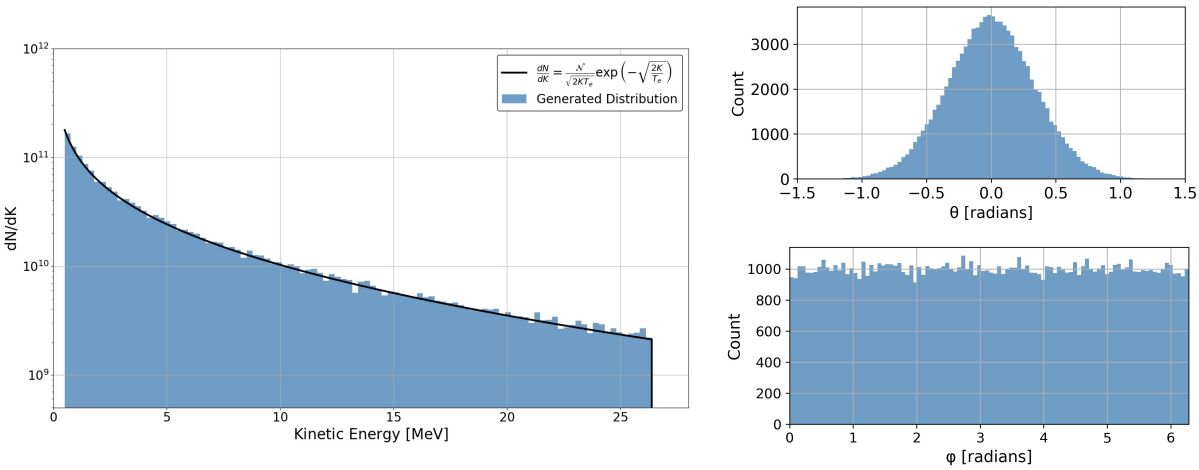

Figure 9: Left: Parametrised energy distribution of laser-driven protons at the LION source. Right: Angular distributions θ (top) and ϕ (bottom).

all particles are contained within $\pm\alpha(E)$ of the z axis for a given energy. The opening angle is observed to decrease as the ion energy increases.

The distribution of the polar angle, θ_S, at which particles are produced at the laser-driven source is generated by defining r' such that

$$r' = \frac{\partial r}{\partial s}\,, \tag{6}$$

where $r = \sin\theta_S$. x' and y' are sampled independently from the probability density function

$$g(r') = \frac{3}{4r'^2_m}\left(r'^2_m - r'^2\right)\,, \tag{7}$$

where $r'_m = \sin\alpha$.

At low kinetic energy ($E \sim E_{min}$), $\alpha(E)$ is taken to be $\sim 20°$. $\alpha(E)$ is assumed to decrease linearly with energy such that

$$\alpha(E) = 20° - 15°\frac{E}{E_{max}}\,, \tag{8}$$

i.e. $\alpha(E)$ decreases from 20° at $E = 0$ to 5° at E_{max}. Finally, the azimuthal angle, ϕ_S, is chosen from a distribution uniform over the range $0 < \phi_S < 2\pi$.

The x and y distributions at production are assumed to be independent and to have inverted parabolic distributions with a maximum spread given by the radius of the laser spot focused on the target.

4.1.3 Source-Generated Electron Background

WThe interactions between the plasma formed when a high-intensity laser strikes a solid target and subsequent laser pulses can lead to the generation of "hot" electrons [31]. These electrons were parametrised using analytical models, following a similar approach to the proton spectra described above, and their transport through the LION beamline and subsequent energy depositions in the SmartPhantom were simulated.

The hot electron energy spectrum follows a Maxwellian distribution:

$$f(E) \sim E^{1/2}\exp\left(-\frac{E}{T_h}\right), \tag{9}$$

with the hot electron temperature defined as

$$T_h = 1.05 \times 10^{-10} I^{0.514}, \tag{10}$$

where E is the electron energy, T_h the hot electron temperature, and I the laser intensity [31]. For the LION facility parameters, T_h is calculated to be approximately 6.53 MeV, corresponding to an electron modal energy of 3.24 MeV.

The angular distribution of hot electrons was modelled by a Gaussian distribution [31]:

$$f(\theta) \sim \exp\left(-\frac{\theta^2}{2\sigma^2}\right), \tag{11}$$

with a standard deviation of $\sigma = 45°$. The emission angle θ is related to the electron Lorentz factor, γ, by

$$\theta = \tan^{-1}\sqrt{\frac{2}{\gamma - 1}}, \tag{12}$$

The azimuthal angle was uniformly distributed between 0 and 2π. For the simulation, it was assumed that one hot electron is generated per proton via the TNSA interaction.

4.1.4 Beamline Modeling

The LION beamline was modeled using the Beam Delivery Simulation (BDSIM) software [32], incorporating quadrupole dimensions, bore diameter, magnetic field strengths, and exit window materials (Kapton and aluminum foils). The simulation was performed in vacuum, with quadrupole drift lengths and collimators (2 mm and 4 mm) configured according to optimized parameters, discussed below, and experimental settings.

4.2 Quadrupole Alignment Optimization

The quadrupole configuration in the BDSIM simulation were optimized to match the patterns observed in the RCF films obtained in the experiment. This was done by ... [**<empty citation>**] ... Misalignment in quadrupole drifts and tilts were investigated to match the observed patterns caused by the proton beams.

...

Table 3: Estimated beamline component settings at the LION beamline for the experimental beam design energies when Stack A (Day 1) was irradiated.

Design Energy [MeV]	**Modal Energy** [MeV]	**Drift 1** [mm]	**Q1 Tilt** [°]	**Drift 2** [mm]	**Q2 Tilt** [°]	**Drift 3** [mm]
12						
16						
20						
20 (repeat)						

Table 4: Estimated beamline component settings at the LION beamline for the experimental beam design energies when Stack B (Day 2) was irradiated.

Design Energy [MeV]	**Modal Energy** [MeV]	**Drift 1** [mm]	**Q1 Tilt** [°]	**Drift 2** [mm]	**Q2 Tilt** [°]	**Drift 3** [mm]
10						
10 (repeat)						
14						
18						

...

4.3 Energy Depositions and Pressure Distribution

A Geant4 simulation of the SmartPhantom was created and the beam parameters at the LION beamline's exit window as given by BDSIM were used as input. Subsequently, the energy depositions of the particles were calculated and written in a three-dimensional matrix. The pressure value at each voxel is calculated based on the energy using Equation 1.

The pressure distribution determines the characteristics of the acoustic signals induced, which have been generated and propagated through space. To ensure that the signals are properly sampled and prevent artefacts in the reconstructed images, a sampling frequency of 90 MHz was selected as a compromise between accuracy and computational speed.

4.4 Acoustic Signal

The three-dimensional energy matrix from Geant4 was used as the source input into k-Wave, to simulate the ion-energy transfer to the medium, the generation of the acoustic waves and their propagation in the three-dimensional space [33] [34].

4.4.1 Acoustic Wave Generation and Propagation

Acoustic measurements of the liquid scintillator indicated a speed of sound of approximately 1474 m/s, a 0.5% reduction compared to pure water [35]. Therefore this value has been used for the simulation.

The waves propagate outwards from the heated regions, with a portion of the acoustic wave originating from the Bragg peak travelling towards the Kapton foil. The Kapton-liquid boundary acts as an interface discontinuity due to the difference in acoustic impedance between the two media [36]. Since there is an acoustic mismatch, with the acoustic impedance of air being much lower than that of the liquid, a larger fraction of the wave is reflected. Consequently, three district waves are detected by the transducers, explaining the peaks in the acoustic traces discussed below.

4.4.2 Detection and Signal Waveforms

In the acoustic simulation, the Olympus V303 transducer and Precision Acoustics ML4X50 Piston hydrophone's limited bandwidth were implemented by applying a Gaussian filter, the centre frequency and bandwidth of which correspond to the transducers' specifications. This ensured that the simulated received waveforms contained only frequency components within the detectable range.

4.5 Optical Simulation

The interior of the SmartPhantom and the imaging optics were simulated using non-sequential ray-tracing in Ansys Zemax OpticStudio version 2025/R1 (Premium). Non-sequential ray-tracing was used in a detailed model of the SmartPhantom in order to determine the image of the scintillating volume including diffuse reflectance from the nominally absorbing surfaces such as the anodized aluminium and the black Kapton. The achromatic doublet lenses had their proprietary anti-reflection coatings included, the BK7 window was uncoated.

Key aspects of the SmartPhantom included were the two optical windows, the proton beam entrance tube and the support ring that holds the Kapton in place. Imaging optics were discussed in Section 2.3.2, and Figure 10 (left) shows the simulated volumes.

A small sample of both the black Kapton film and the black anodized aluminium were measured for both diffuse and specular reflectance using a PerkinElmer LAMBDA 1050+ spectrophotometer. The average reflectance of the diffuse sphere in the 1050+ spectrophotometer was 98.7% over the range 350 nm to 500 nm. Figure 10 (right) shows the diffuse reflectance of our sample of black Kapton. In the optical simulations, the value of 8.2% diffuse reflectance (and thus 91.8 % absorbance) was used which is the measured value at 427 nm. The measured specular reflectance at this wavelength was 2.7% and was not included in the simulation. The black anodized aluminium had a maximum diffuse reflectance of 4.7% over the same range.

The response of a camera imaging an ideally-focused LION beam depositing energy at approximately 20 MeV into the liquid scintillator was simulated. All the simulations use non-sequential ray tracing with both ray splitting and scattering at every surface. The optical sources represent the Monte Carlo predicted intensity of the light from the liquid scintillator are modelled as fifteen elliptical elements each emitting isotropically with intensities and number of photons weighted by the simulated deposited energy in the volume.

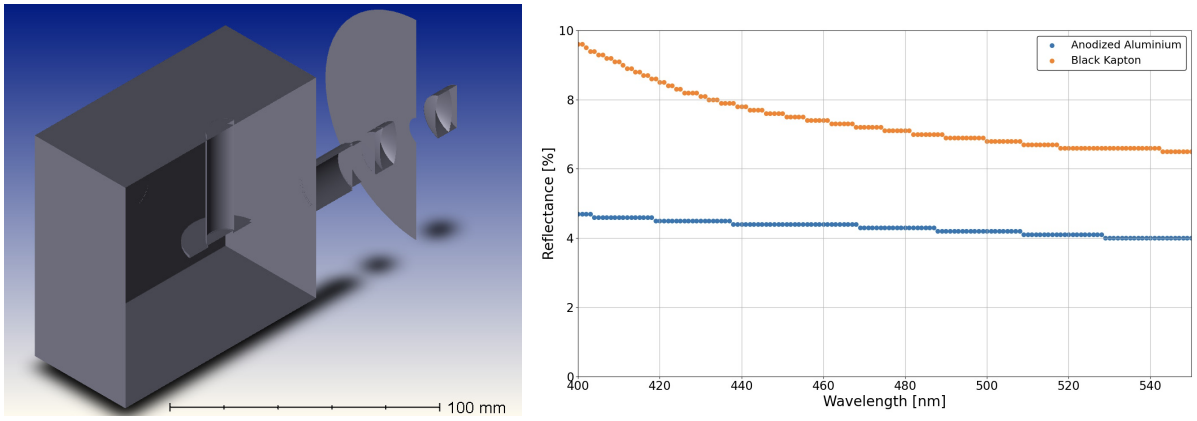

Figure 10: Left: Cut-away 3D volume of the SmartPhantom as simulated in Zemax OpticStudio. Right: Diffuse reflectance of black Kapton (orange) and black anodized aluminium (blue).

Figure 11 shows the result of a simulation where each source has equal intensity. The entrance window port, along with annotated key features, is shown on the left, and the simulated intensity results on the plane of the CMOS camera without (top) and with (bottom) the support ring included in the simulation are shown on the right.

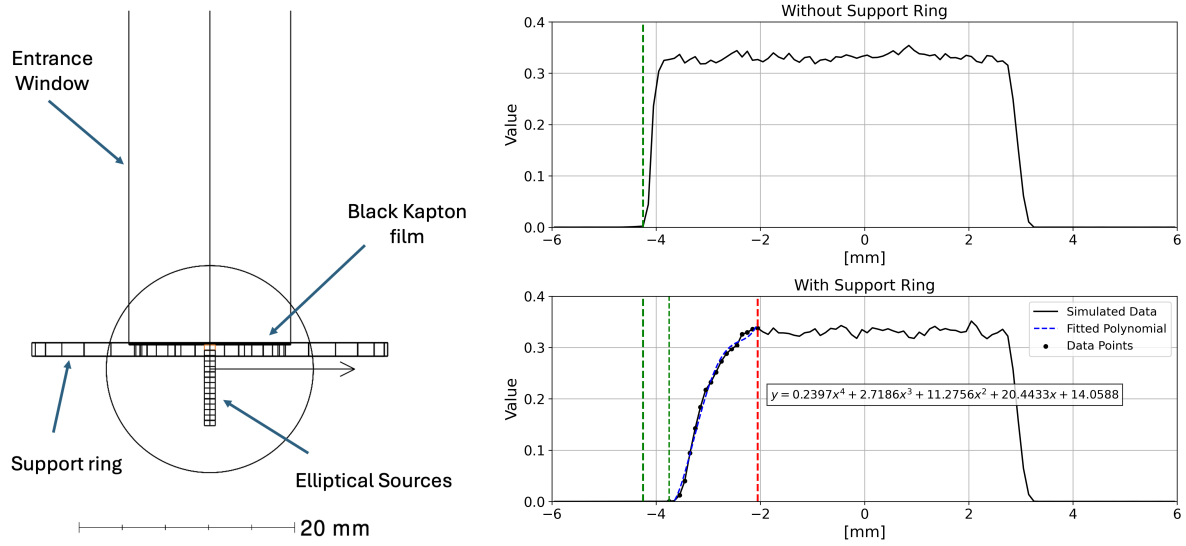

Figure 11: Left: SmartPhantom's entrance window port, black Kapton film, the support ring and the elliptical sources. The arrow points towards the imaging optics and the circle represents the second N-BK7 window with an orthogonal view of the sources. Right: Section along the depth axis for a 0.1 mm diameter uniform set of sources. The first green line corresponds to Kapton foil where the energy depositions begin, the second green line corresponds to the shift in its location when the support ring is included and the red line corresponds to where the shadowing ends.

The total number of primary rays traced was 300 million and a simple Lambertian scattering model was used with three scattered rays produced per scattering event. The minimum relative ray intensity was 0.1% and polarisation and ray splitting at dielectric boundaries was accounted for.

When the support ring is included, the gradient of the rising edge near the Kapton foil is clearly smaller than that of the falling edge. This is due to the support ring partially occluding the light collected from the first 1.5 mm of the emitting source. In addition, the location where the energy depositions are recorded appears shifted (first and second green line), indicating that the first ... are completely occluded. A polynomial fit was applied to the data from that point up to where the occlusion ends (red line).

5 Results and Performance

5.1 Energy Deposition Comparison

The pixel dimensions were converted to millimeters using the physical pixel width of 3.45 μm and the magnification factor of the imaging system, -0.94, determined through the optical simulation discussed in Section 4.5.

Figures 12 and 13 compare the images obtained by the top-view and side-view cameras, to the simulated energy deposition patterns in the corresponding planes using the 4 mm collimator. Similarly, the 2 mm collimator data are shown in Figures 14 and 15.

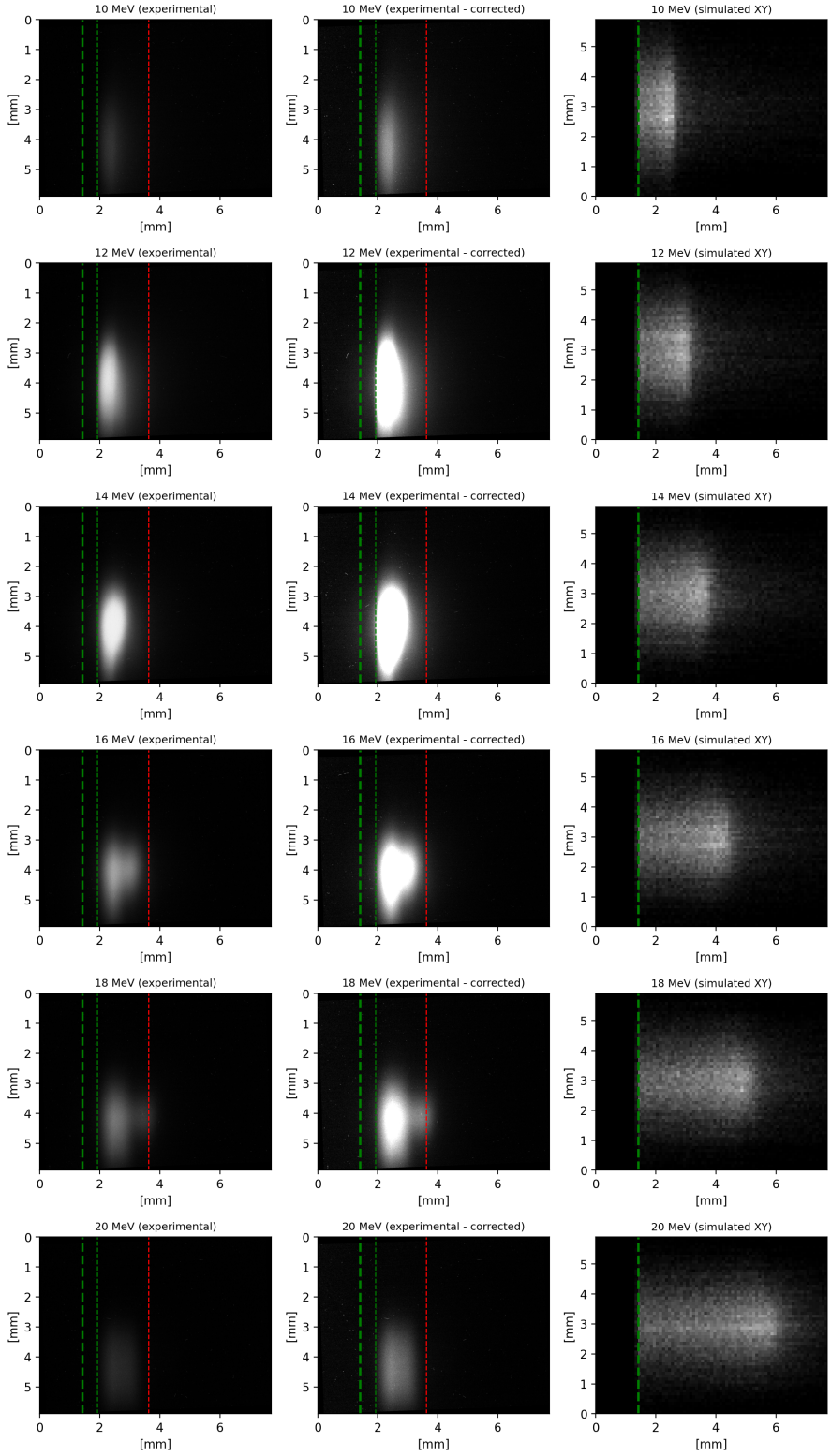

Figure 12: Left: Averaged, background-corrected grayscale images obtained using Camera 2 from the setup shown in Figure 6. Middle: Shadow corrected data using the polynomial fit (max. pixel intensity=256). Right: Simulated energy depositions using BDSIM and Geant4. A 4 mm collimator was placed at the front. Maximum pixel intensity = 256.

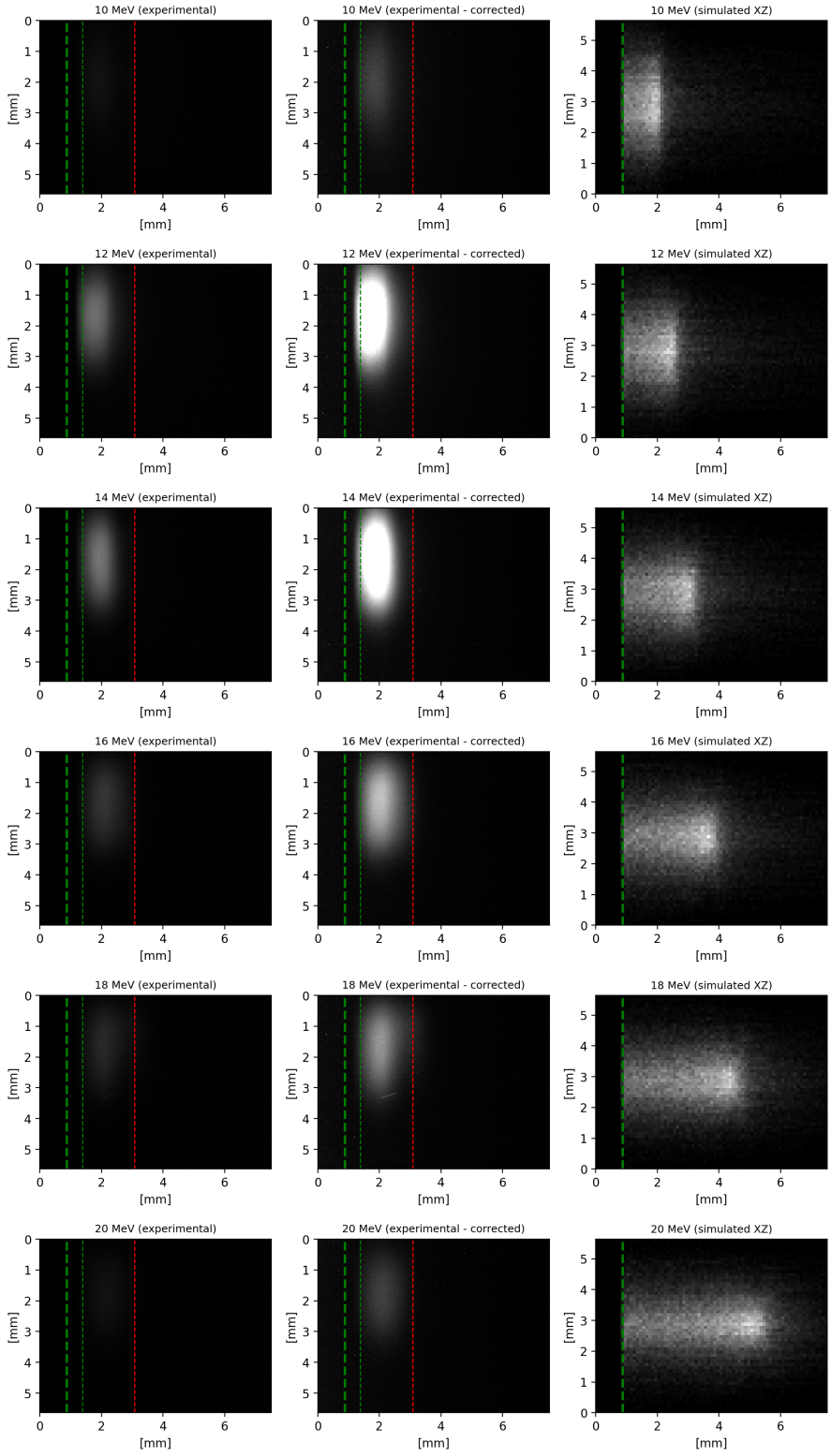

Figure 13: Left: Averaged, background-corrected grayscale images obtained using Camera 2 from the setup shown in Figure 6. Middle: Shadow corrected data using the polynomial fit (max. pixel intensity=256). Right: Simulated energy depositions using BDSIM and Geant4. A 4 mm collimator was placed at the front. Maximum pixel intensity = 256.

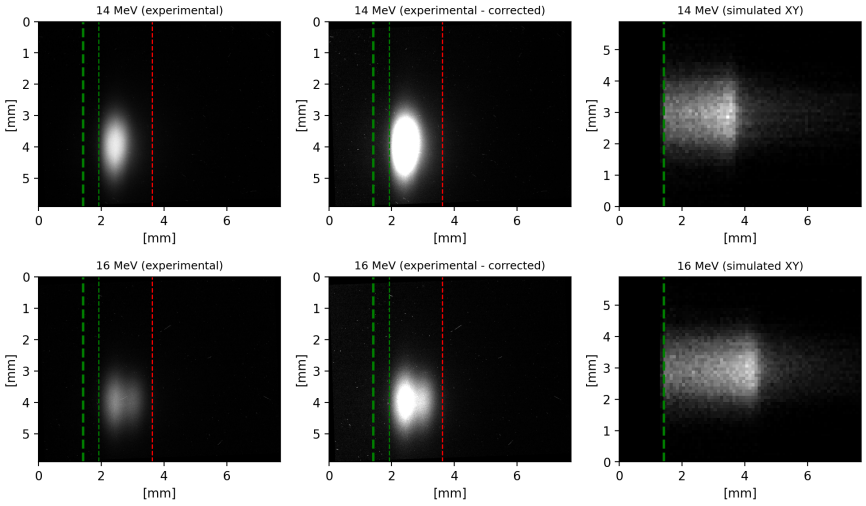

Figure 14: Left: Averaged, background-corrected grayscale images obtained using Camera 2 from the setup shown in Figure 6. Middle: Shadow corrected data using the polynomial fit (max. pixel intensity=256). Right: Simulated energy depositions using BDSIM and Geant4. A 2 mm collimator was placed at the front. Maximum pixel intensity = 256.

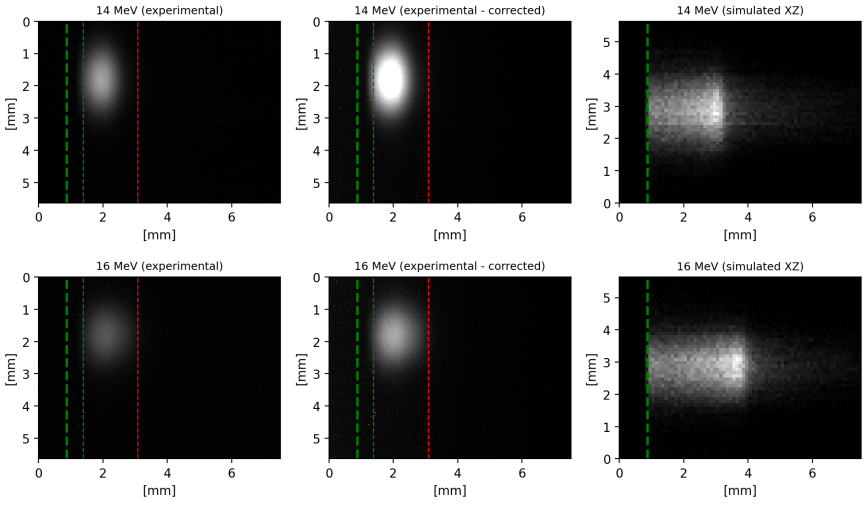

Figure 15: Left: Averaged, background-corrected grayscale images obtained using Camera 2 from the setup shown in Figure 6. Middle: Shadow corrected data using the polynomial fit (max. pixel intensity=256). Right: Simulated energy depositions using BDSIM and Geant4. A 2 mm collimator was placed at the front. Maximum pixel intensity = 256.

5.2 Acoustic Signal Comparison

Simultaneous acoustic measurements were obtained using the Piston hydrophone and Olympus V303 transducer. Before recording the ultrasound signals, acoustic measurements of the background noise, originating from nearby cables and devices, were made. The frequency components of the noise were identified and the transducer signals were filtered to remove them.

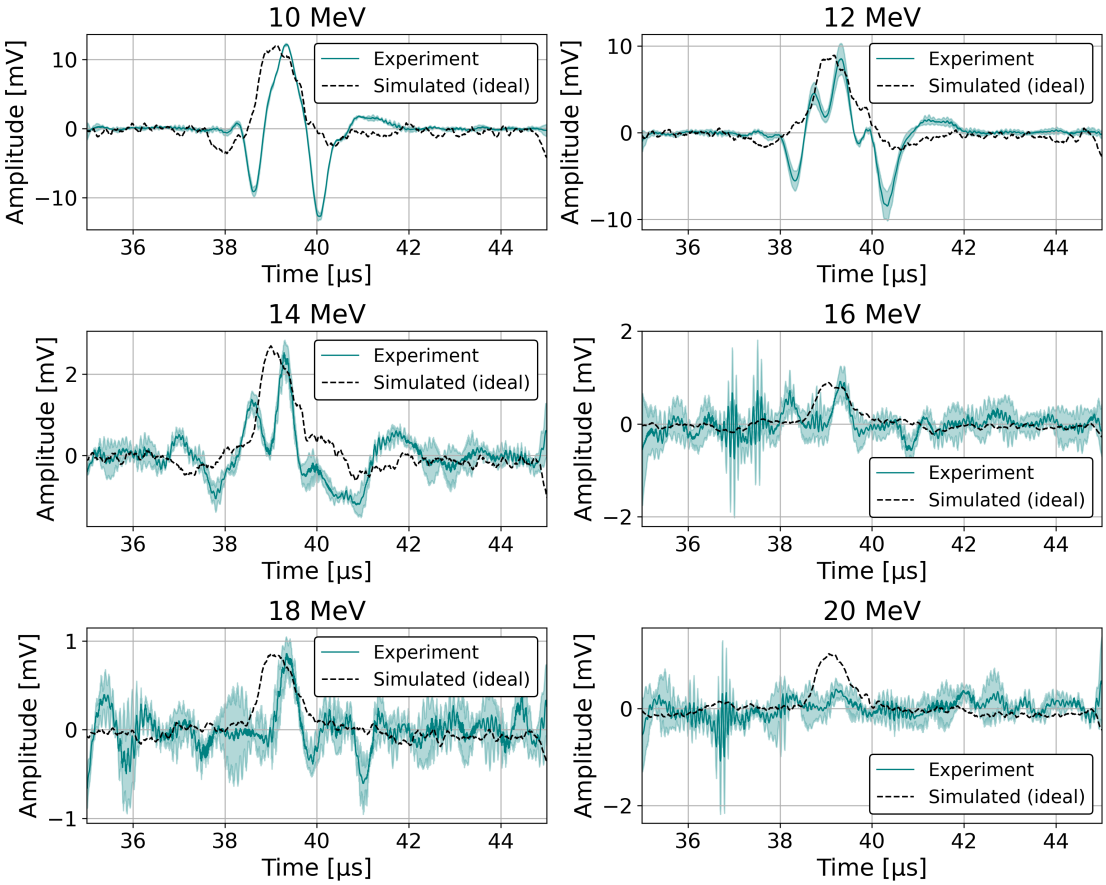

Figure 16: Acoustic waveform recorded by the Piston hydrophone, on-axis with the beam, with a 4 mm collimator placed in front of the SmartPhantom.

6 Discussion

6.1 System Performance

6.2 Limitations and Future Work

6.3 Clinical Outlook

7 Conclusion

8 Acknowledgments

Dr Miles Worsley (Brunel University London) for the diffuse reflectance measurements of anodized aluminium and black Kapton.

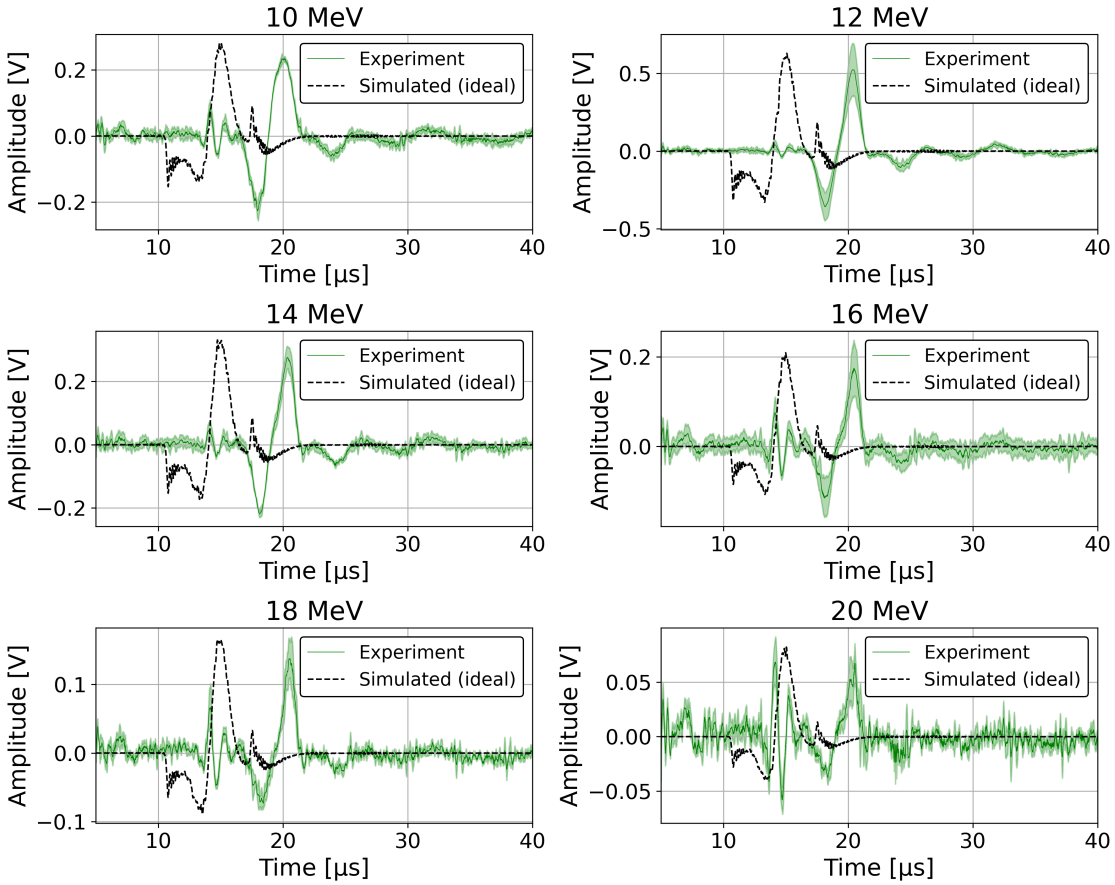

Figure 17: Acoustic waveform recorded by the Olympus V303 transducer, immersed from the bottom, with a 4 mm collimator placed in front of the SmartPhantom.

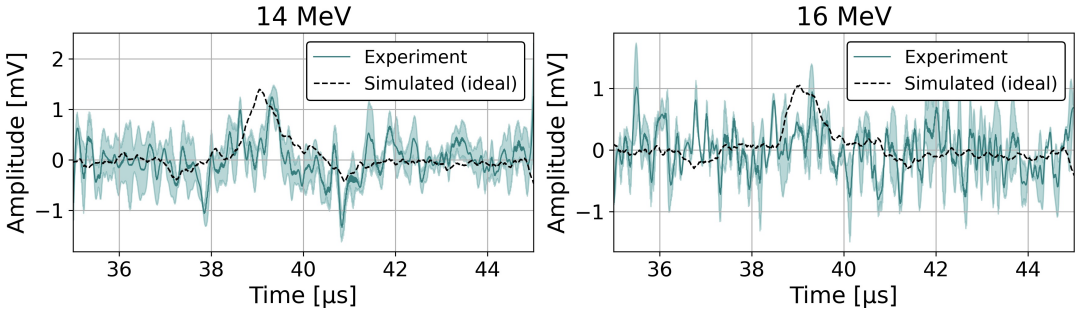

Figure 18: Acoustic waveform recorded by the Piston hydrophone, on-axis with the beam. It's position is shown in Figure 6. A 2 mm collimator was used in this configuration.

References

[1] World Health Organization. *Cancer*. Accessed20 Mar. 2022. 2019. URL: https://www.who.int/health-topics/cancer\#tab=tab_1.

[2] E. V. Maani and C. V. Maani. *Radiation Therapy*. Accessed 2 July 2025. 2022. URL: https://www.ncbi.nlm.nih.gov/books/NBK537036/.

[3] G. Aymar et al. "LhARA: The Laser-hybrid Accelerator for Radiobiological Applications". In: *Frontiers in Physics* 8 (2020), p. 567738. URL: https://doi.org/10.3389/fphy.2020.567738.

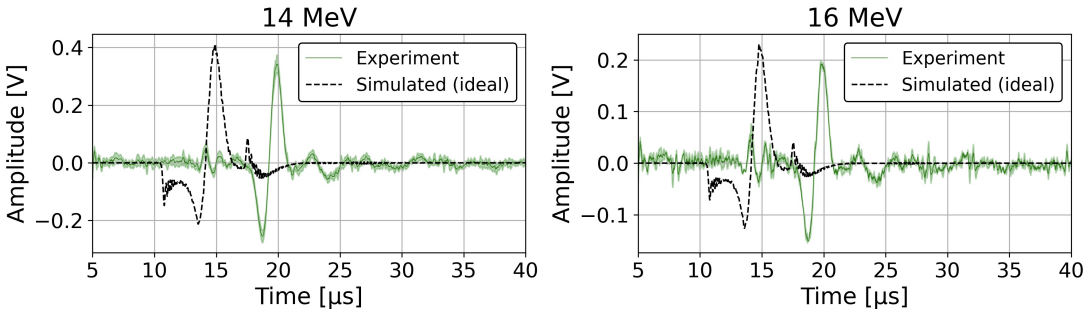

Figure 19: Acoustic waveform recorded by the Olympus V303 transducer, immersed from the bottom. It's position is shown in Figure 6. A 2 mm collimator was used in this configuration.

[4] K. Parodi, W. Enghardt, and T. Haberer. "PET/CT imaging for treatment verification after proton therapy: a study with plastic phantoms and metallic implants". In: *Medical Physics* 34.2 (2007), pp. 419–435. URL: https://doi.org/10.1118/1.2401042.

[5] M. Testa et al. "Dose profile monitoring with carbon ions by means of prompt-gamma measurements". In: *Nuclear Instruments and Methods in Physics Research Section B: Beam Interactions with Materials and Atoms* 267 (2009), pp. 993–996. URL: https://doi.org/10.1016/j.nimb.2009.02.031.

[6] E.J. Lehrer et al. "Proton and Heavy Particle Intracranial Radiosurgery". In: *Biomedicines* 9.1 (2021), p. 31. URL: https://doi.org/10.3390/biomedicines9010031.

[7] T. Nonnenmacher et al. "Anomalous beam transport through Gabor (plasma) lens prototype". In: *Applied Sciences* 11.10 (2021), p. 4357. URL: https://doi.org/10.3390/app11104357.

[8] J. R. Hughes and J. L. Parsons. "FLASH Radiotherapy: Current Knowledge and Future Insights Using Proton-Beam Therapy". In: *International Journal of Molecular Sciences* 21.18 (2020), p. 6492. URL: https://doi.org/10.3390/ijms21186492.

[9] Eshel Faraggi, Shijun Wang, and Bernard Gerstman. "Stress confinement, shock wave formation, and laser-induced damage". In: *Proceedings of SPIE - The International Society for Optical Engineering*. Vol. 5695. 2005. URL: https://doi.org/10.1117/12.589469.

[10] K. C. Jones, W. Nie, J. C. H. Chu, et al. "Acoustic-based proton range verification in heterogeneous tissue: simulation studies". In: *Physics in Medicine Biology* (2018). URL: https://doi.org/10.1088/1361-6560/aa9d16.

[11] *The Physics of Ultrasound – Part 1*. WFSA Resource Library. Accessed 19 May 2024. n.d. URL: https://resources.wfsahq.org/atotw/the-physics-of-ultrasound-part-1/#:~:text=PD%20%3D%20N%20.

[12] X. Chu et al. "Development of novel water equivalent liquid scintillator". In: *Radiation Measurements* 136 (2020), p. 106391. URL: https://doi.org/10.1016/j.radmeas.2020.106391.

[13] T. F. Rösch et al. "Laser-driven ION (LION) acceleration at the Centre for Advanced Laser Applications (CALA)". In: *CLEO/Europe-EQEC*. Munich, Germany, 2017, pp. 1–1. URL: https://doi.org/10.1109/CLEOE-EQEC.2017.8087795.

[14] *ATLAS - Pulse. Petawatt Users, Lasers, Sources and Experiments - LMU Munich*. Accessed 13 Mar. 2023. Mar. 2023. URL: https://www.pulse.physik.uni-muenchen.de/research/high-power/atlas/index.html.

[15] J. Fuchs, P. Antici, E. d'Humières, et al. "Laser-driven proton scaling laws and new paths towards energy increase". In: *Nature Physics* 2 (2006), pp. 48–54. URL: https://doi.org/10.1038/nphys199.

[16] T. F. Rösch et al. "Transverse emittance growth of proton sources from laser-irradiated sub-$ mu$m-thin planar targets". In: *Physical Review E* 109.2 (2024). URL: https://doi.org/10.1103/physreve.109.025201.

[17] *Immersion Transducers*. Accessed 17 Dec. 2024. Dec. 2024. URL: https://www.olympus-ims.com/en/ultrasonic-transducers/immersion/.

[18] *ML4X50 Piston Hydrophone*. Accessed 2 Jun. 2025. June 2025. URL: https://www.acoustics.co.uk/product/piston-hydrophone/.

[19] FEMTO Messtechnik GmbH. *HVA-10M-60-B High Voltage Amplifier*. https://www.femto.de/products/amplifiers/hva-10m-60-b/. Accessed: 2025-07-14. n.d.

[20] FEMTO Messtechnik GmbH. *HQA-15M-10T Charge Amplifier*. https://www.femto.de/products/amplifiers/hqa-15m-10t/. Accessed: 2025-07-14. n.d.

[21] *Ultima Gold XR*. Accessed 2 July 2025.

[22] P G Hoertz et al. "Response of organic liquid scintillators to fast neutrons and gamma radiation". In: *Rad Phy Chem* 84 (2013), pp. 59–86.

[23] K Kossert. "Measurement of wavelength-dependent refractive indices of liquid scintillation cocktails". In: *Appl Rad Iso* 82 (2013), pp. 382–388.

[24] *MC40 Cyclotron Facility - The Birmingham Centre for Nuclear Education and Research*. Accessed 30 Jul. 2024. URL: https://www.birmingham.ac.uk/research/activity/nuclear/about-us/facilities/mc40-cyclotron-facility.

[25] *PicoScope 6404D*. Accessed 16 Feb. 2025. Feb. 2025. URL: https://www.tequipment.net/Pico/6404D/PC-Based-Oscilloscopes/.

[26] P. Casolaro et al. "Real-time dosimetry with radiochromic films". In: *Scientific Reports* 9 (2019), p. 5307. URL: https://doi.org/10.1038/s41598-019-41705-0.

[27] D. J. Walcher. *Absolute Calibration of Radiochromic Films*. Bachelor's thesis, Ludwig Maximilians Universität, Faculty of Physics, Munich. 2021.

[28] J. Schreiber et al. "Analytical model for ion acceleration by high-intensity laser pulses". In: *Physical Review Letters* 97.4 (2006), p. 045005. URL: http://doi.org/10.1103/PhysRevLett.97.045005.

[29] G. Cowan. *Monte Carlo Techniques*. Accessed 2 July 2025. 2019. URL: https://pdg.lbl.gov/2020/reviews/rpp2020-rev-monte-carlo-techniques.pdf.

[30] Python Software Foundation. *Welcome to Python.org*. Accessed 18 Apr. 2022. Apr. 2022. URL: https://www.python.org.

[31] T. T. Liang et al. "Radiation Protection Around High-intensity Laser Interactions with Solid Targets". In: *Health Physics* 115.6 (Dec. 2018), pp. 687–697. URL: https://doi.org/10.1097/HP.0000000000000927.

[32] L. J. Nevay et al. "BDSIM: An accelerator tracking code with particle–matter interactions". In: *Computer Physics Communications* 252 (2020), p. 107200. URL: https://doi.org/10.1016/j.cpc.2020.107200.

[33] *MATLAB - MathWorks*. Accessed 18 Apr. 2022. n.d. URL: https://nl.mathworks.com/products/matlab.html.

[34] *k-Wave: A MATLAB toolbox for the time domain simulation of acoustic wave fields*. Accessed 19 Mar. 2022. n.d. URL: http://www.k-wave.org.

[35] Prof. Peter Hobson and Prof. Jeff Bamber. *Insights on Ultima Gold XR sound speed (personal communication)*. Personal communication, 31 Jul. 2024. 2024.

[36] D. D. Pollock. *Physical Properties of Materials for Engineers*. 2nd ed. CRC Press, 1993. URL: https://doi.org/10.1201/9781003068082.